PCCP

ROYAL SOCIETY OF CHEMISTRY

PAPER

View Article Online
View Journal | View Issue

Check for updates

Cite this: *Phys. Chem. Chem. Phys.*, 2022, **24**, 9345

SAXS data modelling for the characterisation of ion tracks in polymers

Xue Wang,[ab] Shankar Dutt,[b] Christian Notthoff,[b] Alexander Kiy,[b] Pablo Mota-Santiago,[c] Stephen T. Mudie,[c] Maria E. Toimil-Molares,[d] Feng Liu,[ae] Yugang Wang[a] and Patrick Kluth *[b]

Received 21st December 2021,
Accepted 22nd March 2022

DOI: 10.1039/d1cp05813d

rsc.li/pccp

Here, we present new models to fit small angle X-ray scattering (SAXS) data for the characterization of ion tracks in polymers. Ion tracks in polyethylene terephthalate (PET), polycarbonate (PC), polyimide (PI) and polymethyl methacrylate (PMMA) were created by swift heavy ion irradiation using ^{197}Au and ^{238}U with energies between 185 MeV and 2.0 GeV. Transmission SAXS measurements were performed at the Australian Synchrotron. SAXS data were analysed using two new models that describe the tracks by a cylindrical structure composed of a highly damaged core with a gradual transition to the undamaged material. First, we investigate the 'Soft Cylinder Model', which assumes a smooth function to describe the transition region by a gradual change in density from a core to a matrix. As a simplified and computational less expensive version of the 'Soft Cylinder Model', the 'Core Transition Model' was developed to enable fast fitting. This model assumes a linear increase in density from the core to the matrix. Both models yield superior fits to the experimental SAXS data compared with the often-used simple 'Hard Cylinder Model' assuming a constant density with an abrupt transition.

Published on 23 March 2022. Downloaded by Australian National University on 10/23/2023 8:56:24 PM.

1. Introduction

As swift heavy ions penetrate organic and inorganic materials, they mainly interact with the target electrons, and the electronic energy loss is dominant. The resulting ionization and electronic excitations can lead to the formation of narrow, parallel damage trails which are called 'ion tracks'. The formation of continuous tracks requires the electronic energy loss to exceed a material-dependent critical threshold value.[1–4] Affected by the electronic energy loss, energetic secondary electrons, and radial energy deposition, ion tracks generally consist of a small 'track core' with a radius of a few nanometres that is sometimes surrounded by a 'track halo' extending up to a few hundred nanometers.[1–3,5]

Ion tracks in polymers have attracted attention from the scientific community for decades as they have many interesting applications. By chemical etching,[6–10] ion tracks can be converted to nanopores with radii ranging from tens to hundreds of nanometers. Subsequently, these pores can be tuned in size and functionality by atomic layer deposition[11–14] or surface modification.[15–19] These polymer membranes have been used for energetic particle detection,[20,21] nanowire fabrication,[22,23] ion separation,[24,25] gas separation,[26–28] molecule sensing,[12,29–32] energy conversion,[33–36] and response switches or gates.[37–40] The more recently developed track-UV technique enables the fabrication of nanopores in polymer membranes without chemical etching.[11,24,41] The resulting pores have shown effective openings as small as 0.5 nm,[10] achieving both high selectivity and permeability for ion separation.[24,25]

To further advance the applications based on ion tracks in polymers, detailed knowledge of the track structure in polymers and how it depends on the ion irradiation conditions is highly desirable. However, using conventional imaging methods such as transmission electron microscopy (TEM),[42,43] atomic force microscopy (AFM)[44–46] and scanning force microscopy (SFM),[47–49] it is extremely challenging to accurately observe the nanometre scale tracks in polymers due to low contrast, sample charging, and artefacts introduced during sample preparation. Several indirect methods have been used to characterize the track structure in polymers. By chemical etching combined with conductometry, etching curve analysis can provide the size of the 'track core' and 'track halo' but it 'erases' the structure inside the 'track core' during the etching process.[50–52] Ultraviolet-visible spectroscopy (UV-Vis) and

[a] *State Key Laboratory of Nuclear Physics and Technology, School of Physics, Peking University, Beijing 100871, People's Republic of China*
[b] *Department of Materials Physics, Research School of Physics, Australian National University, Canberra ACT 2601, Australia. E-mail: patrick.kluth@anu.edu.au*
[c] *Australian Synchrotron, ANSTO, 800 Blackburn Rd, Clayton, Victoria 3168, Australia*
[d] *GSI Helmholtzzentrum für Schwerionenforschung (GSI), Planckstr. 1, D-64291, Darmstadt, Germany*
[e] *Center for Quantitative Biology, Peking University, Beijing 100871, People's Republic of China*

Published on 23 March 2022. Downloaded by Australian National University on 10/23/2023 8:56:24 PM.

Fourier transform infrared spectroscopy (FTIR) can provide rich information about the damage to the molecular structure in the polymer and can yield an effective damage cross-section of the tracks, yet little information about the track morphology can be deduced.[45,46,53,54]

Synchrotron-based small angle X-ray scattering (SAXS) is a powerful technique for characterizing the structure of ion tracks. SAXS is non-destructive and well suited to analyse the size, shape, and spatial correlation of objects in the nanometre range without special requirements for sample preparation.[55,56] This technique has been successfully applied to study track-etched nanopores[57–61] and ion tracks in polymers and inorganic materials.[57,62–65] One of the most widely used models to fit the SAXS patterns from ion tracks is a simple cylinder approximation. This model has been applied to fit the structure of tracks in polymer samples such as polycarbonate (PC), polyethylene terephthalate (PET) and polytetrafluoroethylene (PTFE) among others.[57,62,63] The so-called 'Hard Cylinder Model' assumes that the ion track has a cylindrical structure with a constant density lower than that of the matrix and an abrupt boundary to the undamaged material. While this model serves as a good approximation, in particular for amorphous tracks in inorganic crystalline materials, it often fails to fit scattering patterns from ion tracks in polymers well. We attribute this to a more complex track structure in polymers that the 'Hard Cylinder Model' does not account for. It is generally accepted that the interaction of secondary electrons with the target material and the energy density deposition are crucial for ion track formation. Swift heavy ions slow down in the target material mainly due to the ionization of target atoms with the emission of secondary electrons. Monte Carlo simulations show a gradual decrease in the radial excited electron density and their energy density in solid materials.[66] In contrast to ion tracks formed in inorganic materials, where the density difference is largely caused by mass redistribution, in polymers, ion track formation is fundamentally different and dominated by bond breaking and outgassing, which reduces with radially decreasing energy deposition and induces the mass loss. For example, the probability for the carbonate ester bond to break gradually decreases in the radial direction away from the ion path.[67] These studies indicate that ion tracks in polymers should have a more complex structure than a simple cylinder with abrupt boundaries, which better describes tracks in inorganic materials.

There are only a few studies using SAXS that have investigated the structure of tracks in polymers to have soft boundaries by assuming either a Gaussian radial density variation[68] or a radial electron density profile consisting of a combination of a hard cylinder and Gaussian distribution.[69,70] The former model does not show any oscillatory behaviour in the scattering pattern while the latter involves an abrupt step in the radial distribution between the hard cylinder and the Gaussian part. These models were unable to explain the scattering observed from our SAXS measurements of ion tracks in polymers. Hence, we developed two new form-factor models termed the 'Soft Cylinder Model' and 'Core Transition Model'. Both models assume that the 'track core' has an inner core region with a constant density followed by a gradual density transition to the 'track halo' with little density change. Given the gradual radial decrease in the deposited energy and concomitant bond breaking efficiency, these models should provide a more realistic description of the radial density variation in the tracks compared to the 'Hard Cylinder Model'.[68–70] This is consistent with previous studies suggesting that a transition zone exists between the 'track core' and the 'track halo'.[71,72]

We performed SAXS measurements of tracks in a variety of polymers such as PET, PC and polyimide (PI), as well as polymethyl methacrylate (PMMA) irradiated with swift heavy ions of ^{197}Au and ^{238}U with energies between 185 MeV and 2.0 GeV. We systematically tested both models and the results indicate that they well reproduce the SAXS measurements of tracks in all polymer samples considered in this study. These new insights may help in gaining a better understanding of the mechanisms involved in track formation.

2. Experimental

Commercially available polymer foils of PET, PC and PI, as well as PMMA thin films deposited on a Si wafer by spin coating (for more details, see Table 1) were irradiated with swift heavy ions at room temperature. The irradiation experiments were performed using ^{197}Au and ^{238}U ions with energies between 1.6 and 2.0 GeV at the UNILAC accelerator at GSI in Germany or 185 MeV ^{197}Au ions at the 14UD accelerator at Australian National University. The fluences ranged from 5×10^{10} to 3×10^{11} ions/ cm^2. Table 1 shows the details of the samples and irradiation conditions. The energy losses dE/dx were calculated using SRIM 2008.[73] Based on the calculations, the ion range by far exceeds the thickness of the polymer foils in all cases, and the electronic energy loss is nearly uniform along the damage trails, *i.e.*, varying by a maximum of 5.7%. Hence, Table 1 lists the electronic energy loss at the surface of the foil.

The tracks in the polymers resulting from ion irradiation were studied by transmission SAXS at the SAXS/WAXS beamline of the Australian Synchrotron in Melbourne, Australia. SAXS measurements were performed with an X-ray energy of 12 keV and detector to sample distances of approximately 1600 mm, 2000 mm, and 3500 mm in different experimental runs. The samples were mounted using a three-axis goniometer which allows the alignment and tilt of the samples to defined angles of the parallel tracks with respect to the X-ray beam to obtain 2D images produced by the detector corresponding to a two-dimensional cut of the tracks in reciprocal space. The measurement geometry is shown in Fig. 1. Images were collected using a Pilatus 1 M or 2 M detector with exposure times of 1 s, 2 s and 5 s. Additionally, pristine samples were measured for the background correction. The distance between the sample and detector was calibrated using a silver behenate reference. To analyse the data, the X-ray scattering intensity was extracted from the streak indicated by the red curve in the 2D image (see Fig. 1). The streak results from the tilt of the aligned cylindrical tracks with respect to X-rays and includes information about the radial density variation in the tracks.[62] The background was chosen by the yellow curve away

 This journal is © the Owner Societies 2022

Published on 23 March 2022. Downloaded by Australian National University on 10/23/2023 8:56:24 PM.

Table 1 Sample information and irradiation parameters

Sample	Thickness (μm)	Trade name	Ion	Ion energy (MeV)	Fluence (ions/ cm^2)	Accelerator	Electronic energy loss at the surface (keV nm^{-1})	Variation of the energy loss across the foil (%)	Projected range (μm)
PET	2	Lumirror, Toray Industries	Au	1635	5×10^{10}	UNILAC, GSI	15.94	0.44	115
PET	2	Lumirror, Toray Industries	Au	185	5×10^{10} 1×10^{11} 3×10^{11}	14UD, ANU	14.36	5.68	25.9
PET	2.8	Rynite, DuPont	Au	1635	1×10^{11}	UNILAC, GSI	15.94	0.50	115
PET	10	Hostaphan, Hoechst	Au	1635	1×10^{11}	UNILAC, GSI	15.94	1.51	115
PET	12	Hostaphan, Hoechst	Au	1635	1×10^{11}	UNILAC, GSI	15.94	1.76	115
PET	19	Hostaphan, Hoechst	Au	1635	1×10^{11}	UNILAC, GSI	15.94	2.63	115
PC	10	Makrofol, Bayer Material Science AG	U	1975	5×10^{10}	UNILAC, GSI	17.62	1.09	126
PI	25	Kapton, DuPont	Au	1635	5×10^{10}	UNILAC, GSI	15.29	4.12	115
PI	25	Kapton, DuPont	U	1975	5×10^{10}	UNILAC, GSI	20.01	2.93	113
PMMA	1.6	Micro resist technology[a]	Au	185	5×10^{10}	14UD, ANU	10.87	3.31	34.4

[a] The thin film of PMMA on the Si wafer was fabricated by spin coating with a PMMA A4 solution (purchased from micro resist technology).

from the polymer ring, but as close as possible without overlapping the streak.[74] After data reduction and background subtraction, the 1D scattering intensity is plotted as a function of the scattering vector q. The resulting 1D scattering pattern contains information about the radial density profile of the ion track.

3. SAXS data modelling

SAXS is a powerful technique to study the size and shape of the ion tracks. The scattering intensity in the SAXS experiment is governed by two factors: the form factor describes the shape and size of the scatterer (ion track), and the structure factor describes the spatial correlation between the ion tracks. The ion tracks fabricated by the irradiation process and investigated in the present study are almost parallel to each other with an average distance far larger than the diameter of the ion tracks themselves. Due to the stochastic nature of ion irradiation, the ion tracks in polymers are randomly distributed over the irradiation surface. This leads to the reduction of the structure factor to 1.[60,75,76] Hence, the scattering intensity $I(\vec{q})$ in the case of ion tracks is directly related to the square of the scattering form factor $f(\vec{q})$ where the scattering vector $\vec{q}$ represents the momentum transfer between the incoming and outgoing waves.[74,77,78]

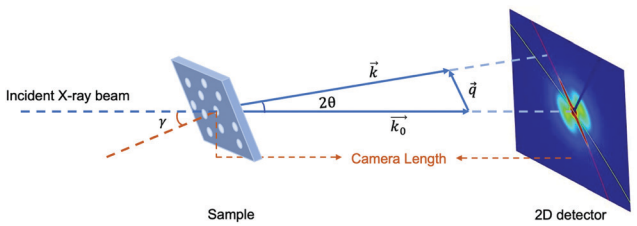

Fig. 1 Schematic of the set-up for transmission SAXS measurements. The ion tracks were tilted by γ with respect to the incoming X-ray beam. The obtained 2D SAXS image of ion tracks in the irradiated PET foil was recorded by the detector. For analysis, the scattering intensity was extracted from the streak along the red curve and the background (extracted along the yellow curve) was subtracted to account for scattering from the matrix.

$$I(\vec{q}) = C|f(\vec{q})|^2 \quad (1)$$

The pre-factor C contains information about the number density of the scatterers and intensity calibration and is considered as a scaling factor in the fitting process. We assume that the polymers are isotropic materials and the tracks possess cylindrical symmetry and translational symmetry along the axis. The latter assumption is justified given that the electronic energy loss is almost uniform across the thickness of the polymer, and the nuclear energy loss is negligible. The scattering form factor $f(\vec{q})$ is obtained by performing a Fourier transform of the scattering object (ion track) and can be expressed in cylindrical coordinates as follows:[61,65,75,79]

$$f(\vec{q}) = 2\pi \frac{\sin(q_z L/2)}{q_z/2} \int_0^\infty r\Delta\rho(r) J_0(q_r r)\mathrm{d}r, \quad (2)$$

where L is the length of the ion tracks, which is equal to the thickness of the membrane, and J_0 is the zero-order Bessel function. q_r and q_z are the radial component and z-component of the scattering vector and can be expressed as $q\cos\theta$ and $q\sin\theta$, respectively, where θ is the half scattering angle. The function $\Delta\rho(r)$ describes the radial electron density change in the cylindrical ion tracks compared to the matrix of the polymers. Considering the half-length of the nanopore $l = L/2$, eqn (2) is reduced to

$$f(\vec{q}) = 2\pi \frac{\sin(q\sin(\theta)l)}{q\sin(\theta)/2} \int_0^\infty r\Delta\rho(r) J_0(q\cos(\theta)r)\mathrm{d}r \quad (3)$$

Published on 23 March 2022. Downloaded by Australian National University on 10/23/2023 8:56:24 PM.

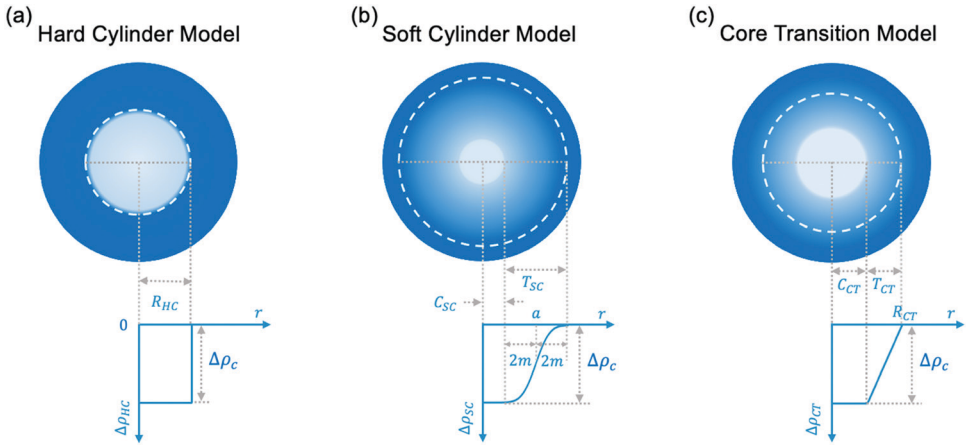

Fig. 2 SAXS fitting models for analysing the radial electron density distribution of cylindrical ion tracks in polymers: (a) Hard Cylinder Model, (b) Soft Cylinder Model and (c) Core Transition Model. White dashed circles indicate the boundary of the tracks, where the density corresponds to that of the unirradiated material. The graph in the bottom row shows the radial density profile of the different models. The point *a* is the midpoint in the transition region of the soft cylinder model in (b).

Many studies have considered the radial density of the damage region to be constant with an abrupt transition to the undamaged material.[57,62–65] This so-called 'Hard Cylinder Model' assumes that the ion track is a simple cylinder with a radius R and has a constant density lower than that of the matrix material (Fig. 2a). Hence, by assuming $\Delta\rho(r)$ to be a constant, the integral in eqn (3) has an analytical solution and the form factor for the Hard Cylinder Model can be written as:

$$f_{\mathrm{HC}}(\vec{q}) = 4\pi\Delta\rho_{\mathrm{c}}\frac{\sin(q\sin(\theta)l)}{q^2\sin(\theta)\cos(\theta)}R_{\mathrm{HC}}J_1(q\cos(\theta)R_{\mathrm{HC}}), \qquad (4)$$

where R_{HC} is the track radius, J_1 is the first-order Bessel function, and $\Delta\rho_{\mathrm{c}}$ is the constant density change. This simple model provides a good approximation of the scattering data of ion tracks in many materials (including polymers[57,62,63]). For etched tracks in polymers, it is clearly a very good representation of the true structure; however, for un-etched tracks in polymers, the track structure is more complex considering the realistic density profile discussed in the last section, and the Hard Cylinder Model only provides a crude approximation. Interestingly, it has been found that the fitting to the SAXS data of un-etched tracks can be improved by introducing a phenomenological parameter describing the 'roughness' of the scattering object as an exponential attenuation factor.[57,60,80] With this addition, the scattering intensity of the Hard Cylinder Model is defined as follows:

$$|I_{\mathrm{HC}}(\vec{q})| \propto |f_{\mathrm{HC}}(\vec{q})|^2\cdot e^{-\sigma_{\mathrm{D}}^2q^2} \qquad (5)$$

The variable σ_{D} is used as a fitting parameter and defines the damping of the scattering intensity. This 'roughness' parameter has been interpreted as a measure of unevenness at the track boundary; however, it is questionable if this parameter appropriately describes the structure of the un-etched tracks in polymers.

In this study, to directly model a more realistic density change between the damaged core and the matrix of the ion tracks in polymers, we developed a new form factor model called 'Soft Cylinder Model', which involves a constant density change in the core region and a gradual density change from the core to the un-damaged matrix. The radial density profile of the soft cylinder model is defined using the modified error function and is shown in Fig. 2b:

$$\Delta\rho_{\mathrm{SC}}(r) = \frac{\Delta\rho_{\mathrm{c}}}{2}\cdot\left(\mathrm{erf}\left(\frac{r-a}{m}\right)-1\right)$$
$$= \frac{\Delta\rho_{\mathrm{c}}}{2}\cdot\left(\frac{2}{\sqrt{\pi}}\int_0^{\left(\frac{r-a}{m}\right)}e^{-t^2}\mathrm{d}t-1\right), \qquad (6)$$

where $\Delta\rho_{\mathrm{c}}$ is the constant density change in the core region. The variables a and m in eqn (6) define the midpoint and the slope of the curved region, respectively. As illustrated in Fig. 2b, the curve is divided into two parts: the constant density region is defined as the core region and the region representing the gradual change in the density distribution referred to as the transition region. Using these variables, we can define the core region (C_{SC}) and the transition region (T_{SC}) of the Soft Cylinder Model as follows:

$$C_{\mathrm{SC}} = a - 2m$$

$$T_{\mathrm{SC}} = 4m$$

The effective radius of the track is defined as $R_{\mathrm{SC}} = a$, *i.e.*, the point in the transition region where the density difference decreases to half of the total density change. Using values from eqn (6) in eqn (3), we obtain the form factor for the Soft Cylinder Model:

$$f_{\mathrm{SC}}(\vec{q}) = 2\pi\Delta\rho_{\mathrm{c}}\frac{\sin(q\sin(\theta)l)}{q\sin(\theta)}\int_0^{\infty}r\cdot\left(\mathrm{erf}\left(\frac{r-a}{m}\right)-1\right)J_0(q\cos(\theta)r)\mathrm{d}r \qquad (7)$$

The soft cylinder model can be successfully applied to fit the data which cannot be fit by the Hard Cylinder Model as outlined below. However, this model is computationally

 This journal is © the Owner Societies 2022

Published on 23 March 2022. Downloaded by Australian National University on 10/23/2023 8:56:24 PM.

relatively expensive and requires significant time to process large amounts of data as eqn (7) does not have an analytical solution and its integration needs to be performed numerically.

As an alternative, we also introduce a simpler approximation to the Soft Cylinder Model, defined as the 'Core Transition Model', which is also an improvement over the Hard Cylinder Model. Fig. 2c shows the electron density distribution of the Core Transition Model. As illustrated in the figure, the core region (C_{CT}) has a constant density change $\Delta\rho_c$. The transition region (T_{CT}) is represented by a linear density change. The slope m and y-intercept c of the transition region are given by:

$$m = \frac{\Delta\rho_c}{C_{CT} - R_{CT}} \quad \text{and } c = \Delta\rho_c - mC_{CT} = \frac{\Delta\rho_c R_{CT}}{R_{CT} - C_{CT}}. \tag{8}$$

The electronic density distribution profile for the Core Transition Model can thus be written as follows:

$$\Delta\rho_{CT}(r) = \begin{cases} \Delta\rho_c & 0 < r \le C_{CT} \\ \left(\frac{\Delta\rho_c}{C_{CT} - R_{CT}}\right) r + \frac{\Delta\rho_c R_{CT}}{R_{CT} - C_{CT}} & C_{CT} < r \le R_{CT} \\ 0 & R_{CT} < r \end{cases} \tag{9}$$

Inserting the density profile defined in eqn (9) into eqn (3), we obtain the form factor for the Core Transition Model:

$$\begin{aligned} f_{CT}(\vec{q}) =& 2\pi \frac{\sin(q\sin(\theta)l)}{q\sin(\theta)/2}\left(\int_0^{C_{CT}} r\Delta\rho_c J_0(q\cos(\theta))\mathrm{d}r\right. \\ &+ \int_{C_{CT}}^{R_{CT}} \left(\left(\frac{\Delta\rho_c}{C_{CT} - R_{CT}}\right) r + \frac{\Delta\rho_c R_{CT}}{R_{CT} - C_{CT}}\right) \\ &\left.\times\ J_0(q\cos(\theta))\mathrm{d}r\right) \end{aligned} \tag{10}$$

This equation can be further simplified to

$$\begin{aligned} f_{CT}(\vec{q}) \ =& 4\pi \frac{\sin(q\sin(\theta)l)}{q\sin(\theta)} \frac{1}{(q\cos(\theta))^2}\pi(-C_{CT}J_1(C_{CT}q\cos(\theta)) \\ &\times \boldsymbol{H}_0(C_{CT}q\cos(\theta)) + R_{CT}J_1(R_{CT}q\cos(\theta))\boldsymbol{H}_0 \\ &(R_{CT}q\cos(\theta)) + C_{CT}J_0(C_{CT}q\cos(\theta))\boldsymbol{H}_1(C_{CT}q\cos(\theta)) \\ &- R_{CT}J_0(q\cos(\theta)R_{CT})\boldsymbol{H}_1(q\cos(\theta)R_{CT})), \end{aligned} \tag{11}$$

where J_1 is the Bessel function of the first-order and $H_u(z)$ is the Struve function defined as follows:

$$H_u(z) = \left(\frac{1}{2}z\right)^{u+1} \sum_{m=0}^{\infty} \frac{(-1)^m \left(\frac{1}{2}z\right)^{2m}}{\Gamma\left(m + \frac{3}{2}\right)\Gamma\left(m + u + \frac{3}{2}\right)}$$

Since the tracks are generated from the same damage process, they are highly monodisperse with very narrow size distributions. Differences between tracks can however arise due to factors like energy straggling and range straggling caused by electronic and nuclear collisions. This leads to an effective narrow size distribution of the tracks. We consider this variation by implementing a narrow Schulz–Zimm distribution,[61,74,75] which is very similar to a Gaussian distribution for small values of the dispersity but has the added advantage that it does not have negative values that are non-physical for track radii. The standard deviation or the width of the distribution defines the dispersity in the radius values. With this modification, the scattering intensity for the models defined earlier can be written as follows:

$$I(\vec{q}) = C\int_0^{\infty} p(R_0, R)\mathrm{d}R|f(\vec{q}, R, L)|^2 \tag{12}$$

with,

$$p(R_0, R) = \frac{1}{\mathrm{Norm}}(z+1)^{z+1}\left(\frac{R}{R_0}\right)^z \frac{\exp(-(z+1)R/R_0)}{R_0\Gamma(z+1)} \tag{13}$$

where Norm is the normalization factor. The variable z defines the width of the distribution

$$z = \frac{1 - \sigma^2}{\sigma^2},$$

where σ is the dispersity parameter used in the fitting model given by

$$\sigma = \frac{p'}{R_0},$$

where R_0 is the mean of the distribution and p' is the root mean square deviation from R_0. The size distribution of the transition region for both the Soft Cylinder Model and the Core Transition Model (T_{SC} and T_{CT}) with a mean value of t_{SC} and t_{CT} is fixed by scaling the distribution applied on C_{SC} and C_{CT} to t_{SC}/R_0 and t_{CT}/R_0, respectively. While deriving the scattering form factor for all the models, we have considered that all ion tracks are parallel to each other, but this is not necessarily the case. A small angular spread due to a small ion-beam divergence during irradiation and because the thin polymer foils may not be entirely flat during irradiation or during the SAXS measurements are realistic assumptions. To account for this, we implement a small constant angular distribution, with ω being used as a fit parameter:

$$I'(\vec{q}) = \frac{\int_0^{\omega} I(\vec{q})\sin\theta\mathrm{d}\theta}{\int_0^{\omega}\sin\theta\mathrm{d}\theta} \tag{14}$$

Here, $I'(\vec{q})$ defines the scattering intensity resulting from the angularly distributed scatterers, with small angular dispersion ω. In summary, the scattering intensities from the nanopores defined using our Soft Cylinder Model $\left(I'_{SC}(\vec{q})\right)$ and core transition model $\left(I'_{CT}(\vec{q})\right)$ are given as follows:

$$\begin{aligned} I'_{SC}(\vec{q}) \ =& \frac{C}{\int_0^{\omega}\sin\theta\mathrm{d}\theta}\int_0^{\omega}\int_0^{\infty}\left|2\pi\rho_0\frac{\sin(q\sin(\theta)l)}{q\sin(\theta)}\int_0^{\infty} r\right. \\ &\left.\cdot\left(\mathrm{erf}\left(\frac{r-a}{m}\right) - 1\right)J_0(q\cos(\theta)r)\mathrm{d}r\right|^2 \\ &\times p(c_{SC}, C_{SC})\mathrm{d}C_{SC}\sin\theta\mathrm{d}\theta + I_{bkg} \end{aligned} \tag{15}$$

Published on 23 March 2022. Downloaded by Australian National University on 10/23/2023 8:56:24 PM.

$$I'_{CT}(\vec{q}) = \frac{C}{\int_0^{\omega}\sin\theta \mathrm{d}\theta}\int_0^{\omega}\int_0^{\infty}\left|4\pi\frac{\sin(q\sin\theta l)}{q\sin\theta}\frac{1}{q^2\cos^2\theta}\right.$$
$$\times\ \pi(-C_{CT}J_1(C_{CT}q\cos\theta)\boldsymbol{H}_0(C_{CT}q\cos\theta)$$
$$+ R_{CT}J_1(R_{CT}q\cos\theta)\boldsymbol{H}_0(R_{CT}q\cos\theta)$$
$$+ C_{CT}J_0(C_{CT}q\cos\theta)\boldsymbol{H}_1(C_{CT}q\cos\theta) \quad (16)$$
$$\left.- R_{CT}J_0(q\cos\theta R_{CT})\boldsymbol{H}_1(q\cos\theta R_{CT}))\right|^2$$
$$\times\, p(c_{CT}, C_{CT})\mathrm{d}C_{CT}\sin\theta\mathrm{d}\theta + I_{bkg},$$

where c_{SC} and c_{CT} are the mean values of the core radius for the Soft Cylinder Model and the Core Transition Model. The term I_{bkg} is included to account for a constant background.

4. Results and discussion

4.1 Track structure in PET

Before applying the newly developed form factor models, *i.e.* the Soft Cylinder Model and the Core Transition Model, to fit the experimental data, we show how the corresponding SAXS patterns differ from those of the Hard Cylinder Model. For comparison, we calculated the scattering intensities of the three models as shown in Fig. 3 with the track structure parameters shown in Table 2 and the corresponding radial density profiles in the inset of Fig. 3. The three different track structures share the same amount of the total mass loss, and the same effective radii. For the Hard Cylinder Model, the definition of the radius is straight forward and is the radius of the constant low-density region. For the Soft Cylinder Model and the Core Transition Model, the effective track radius can be defined as the core plus half of the transition region. Notably, the slope of the transition region in the 'core-transition' track nearly overlaps with the curve of the transition region of the 'soft-cylinder' track. No distributions in size or angle were assumed. As shown in Fig. 3, the SAXS pattern calculated with the Hard Cylinder Model is different from those calculated with the new models considering a transition region. The difference is mainly manifested in the slope at higher q and a slight chirp of the oscillations. We also observe that the SAXS pattern calculated with the Core Transition Model is very similar to that of the Soft Cylinder Model for the first two oscillations. As we generally observe only one oscillation experimentally for ion tracks in polymers, the Core Transition Model and the soft cylinder model are expected to yield very similar fitting results to the SAXS patterns. The differences in the two models may thus only be revealed if a better signal to noise ratio can be achieved in the experimental data that exhibit at least 3 oscillations. Given the position of the first oscillation is similar in all three models, it can also be understood that the hard cylinder model yields a good approximation for determining the track radii.

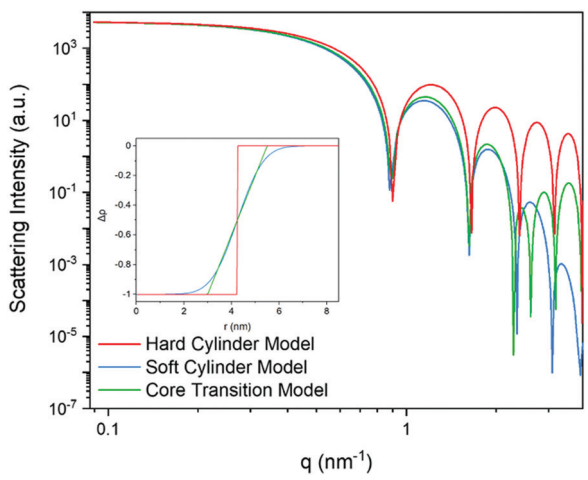

Fig. 3 Comparison of the SAXS patterns calculated using the Soft Cylinder Model, the Core Transition Model and the Hard Cylinder Model assuming that they share the same effective track radius. The inset shows the corresponding radial density profiles of these models.

Table 2 Parameters for the Soft Cylinder Model, Core Transition Model and Hard Cylinder Model plotted in Fig. 3. The 'radius' refers to the effective track radius, which is defined as the core plus half of the transition region in the Soft Cylinder Model and Core Transition Model

Model	Core (nm)	Transition (nm)	Radius (nm)
Hard cylinder	4.25	0.00	4.25
Soft cylinder	1.80	4.90	4.25
Core transition	3.00	2.50	4.25

Fig. 4 shows the SAXS scattering patterns from ion tracks in 2 μm-thick PET irradiated with 185 MeV Au ions as well as the fits to the different models discussed in the previous section. The fitting parameters are listed in Table 3. As apparent in Fig. 4a, the best fit of the Hard Cylinder Model shows a significant deviation from the data, suggesting that a more complex structure needs to be taken into consideration. With the addition of a phenomenological roughness parameter in the Hard Cylinder Model (Fig. 4b),[57,63] we can obtain a better fit but a small chirp is still apparent as also observed in the model comparison in Fig. 3.

A more realistic track structure is expressed in the Soft Cylinder Model (Fig. 4c) which fits the SAXS data very well and can give us a better description of the track structure than the Hard Cylinder Model with the roughness parameter. However, in the actual fitting process, this model is relatively computationally expensive as we discussed in the previous section. Hence, we developed the Core Transition Model as a 'faster' alternative. In our software implementation, the computation time of the Core Transition Model was at least 10 times shorter than that of the Soft Cylinder Model. The fit to the data in Fig. 4d using the Core Transition Model is also very good. Comparing the density plot (in the inset) between the soft cylinder and Core Transition Models, we see they deliver very similar results.

All fitting parameters of the polymer samples with the different models mentioned in this paper are listed in Table 3. Uncertainties of the fitting parameters including the core, transition, polydispersity, and angle were estimated from the fittings. Strong oscillations in the scattering intensities lead to smaller values for the polydispersity and indicate a narrow distribution of the track size.

 This journal is © the Owner Societies 2022

Published on 23 March 2022. Downloaded by Australian National University on 10/23/2023 8:56:24 PM.

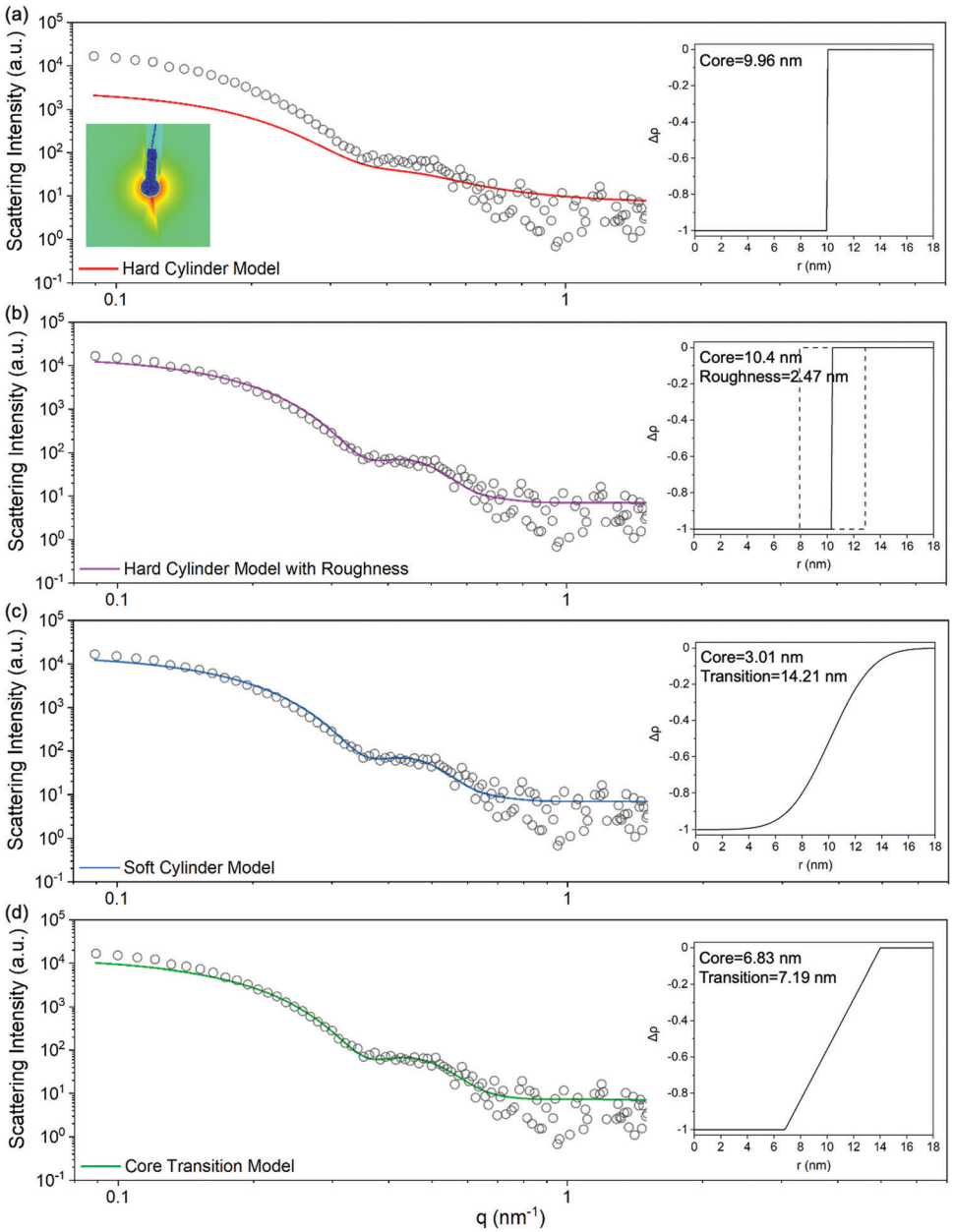

Fig. 4 SAXS patterns (circles) and corresponding fits using different models (solid lines) for 2 μm-thick PET irradiated with 185 MeV Au at 1×10^{11} ions/cm^2: (a) Hard Cylinder Model, (b) Hard Cylinder Model with roughness, (c) Core Transition Model, and (d) Soft Cylinder Model. The insets are the 2D SAXS detector image (on the left in a), and the radial electron density profile from each model fit (on the right).

As we discussed in the previous section, considering the ion beam divergence during irradiation or the bending of the thin foil samples when mounted on the sample holder, it may cause the ion tracks not to be parallel anymore during the irradiation experiments or during SAXS measurements. The addition of an angular distribution provides a better fit to the data (Fig. 5a), yet the track radius remains unaffected, and the transition regions as well as the core regions only change slightly within errors (Fig. 5b). Therefore, in the following, we add the angular distribution to all the models to improve the fits to the data.

We further test the suitability of the new models in three different PET samples including 2 μm-thick PET irradiated with 185 MeV Au at 1×10^{11} ions/cm^2, 19 μm-thick PET irradiated with 1635 MeV Au at 1×10^{11} ions/cm^2, and 2 μm-thick PET irradiated with 1635 MeV at 5×10^{10} ions/cm^2. As expected, the Core Transition Model and Soft Cylinder Model with angular distribution can fit the structure of tracks in PET well for different thicknesses and irradiation conditions (Fig. 6a–c). In contrast, the Hard Cylinder Model with roughness does not fit the data very well for all the samples due to the limitations discussed earlier. The fitting parameters for the PET samples using the hard cylinder, core transition and Soft Cylinder Models are listed in Table 3. Fig. 7a–c show the radial density profiles from the fits to all models for the three tested samples.

Published on 23 March 2022. Downloaded by Australian National University on 10/23/2023 8:56:24 PM.

Table 3 Fitting results from the SAXS analysis using all models mentioned in this paper. The 'radius' refers to the effective track radius, which is defined as the core plus half of the transition in the core transition and Soft Cylinder Model

Model	Polymer	Thickness (μm)	Ion	Energy (MeV)	Fluence (ions/cm^2)	Energy loss (keV nm^{-1})	Core (nm)	Transition (nm)	Radius R (nm)	Dispersity $[\sigma]$ (nm)	Roughness $[\sigma_D]$ (nm)	Angle (°)
Hard cylinder	PET	2	Au	185	1×10^{11}	14.36	9.96 ± 2.20	—	9.96 ± 2.20	0.23 ± 0.16	—	—
	PET	2	Au	1635	5×10^{10}	15.92	4.19 ± 0.21	—	4.19 ± 0.21	0.24 ± 0.04	—	—
	PET	19	Au	1635	1×10^{11}	15.92	4.34 ± 0.15	—	4.34 ± 0.15	0.16 ± 0.03	—	—
Hard cylinder with roughness	PET	2	Au	185	1×10^{11}	14.36	10.43 ± 0.81	—	10.43 ± 0.81	0.13 ± 0.06	2.47 ± 0.46	—
	PET	2	Au	1635	5×10^{10}	15.92	4.41 ± 0.05	—	4.41 ± 0.05	0.16 ± 0.01	1.50 ± 0.03	—
	PET	19	Au	1635	1×10^{11}	15.92	3.91 ± 0.04	—	3.91 ± 0.04	0.16 ± 0.01	1.11 ± 0.01	—
Hard cylinder with angle	PET	2	Au	185	1×10^{11}	14.36	10.40 ± 1.33	—	10.40 ± 1.33	0.18 ± 0.09	—	0.62 ± 0.00
	PET	2	Au	1635	5×10^{10}	15.92	4.22 ± 0.02	—	4.22 ± 0.02	0.18 ± 0.01	—	0.47 ± 0.00
	PET	19	Au	1635	1×10^{11}	15.92	3.54 ± 0.04	—	3.54 ± 0.04	0.18 ± 0.01	—	0.50 ± 0.01
Soft cylinder	PET	2	Au	185	1×10^{11}	14.36	3.01 ± 1.63	14.21 ± 2.72	10.12 ± 2.99	0.08 ± 0.04	—	—
Soft cylinder with angle	PET	2	Au	185	1×10^{11}	14.36	3.01 ± 1.64	14.19 ± 2.73	10.11 ± 3.01	0.08 ± 0.04	—	0.02 ± 0.00
	PET	2	Au	1635	5×10^{10}	15.92	1.15 ± 0.10	5.91 ± 0.18	4.11 ± 0.19	0.11 ± 0.01	—	0.72 ± 0.00
	PET	19	Au	1635	1×10^{11}	15.92	1.13 ± 0.16	5.27 ± 0.20	3.77 ± 0.26	0.10 ± 0.01	—	0.31 ± 0.04
Core transition	PET	2	Au	185	1×10^{11}	14.36	6.83 ± 1.07	7.19 ± 1.41	10.43 ± 1.78	0.13 ± 0.06	—	—
	PET	19	Au	1635	1×10^{11}	15.92	2.65 ± 0.19	3.00 ± 0.14	4.15 ± 0.26	0.18 ± 0.02	—	—
Core transition with angle	PET	2	Au	185	5×10^{10}	14.36	6.34 ± 0.80	7.10 ± 1.55	9.89 ± 1.58	0.11 ± 0.02	—	0.34 ± 0.10
	PET	2	Au	185	1×10^{11}	14.36	7.19 ± 1.13	6.54 ± 1.66	10.46 ± 1.96	0.13 ± 0.06	—	0.20 ± 0.00
	PET	2	Au	185	3×10^{11}	14.36	9.01 ± 0.28	4.60 ± 0.16	11.31 ± 0.36	0.20 ± 0.02	—	0.01 ± 0.00
	PET	2	Au	1635	5×10^{10}	15.92	3.03 ± 0.07	2.29 ± 0.14	4.18 ± 0.14	0.19 ± 0.01	—	0.42 ± 0.00
	PET	2.8	Au	1635	1×10^{11}	15.92	3.07 ± 0.27	2.60 ± 0.39	4.37 ± 0.47	0.17 ± 0.04	—	0.15 ± 0.00
	PET	10	Au	1635	1×10^{11}	15.92	2.85 ± 0.03	2.41 ± 0.04	4.06 ± 0.05	0.15 ± 0.00	—	0.07 ± 0.00
	PET	12	Au	1635	1×10^{11}	15.92	2.74 ± 0.27	2.86 ± 0.33	4.17 ± 0.44	0.12 ± 0.03	—	0.04 ± 0.00
	PET	19	Au	1635	1×10^{11}	15.92	2.84 ± 0.13	2.43 ± 0.12	4.06 ± 0.19	0.16 ± 0.02	—	0.02 ± 0.00
	PC	10	U	1975	5×10^{10}	17.62	1.98 ± 0.25	2.37 ± 0.44	3.17 ± 0.47	0.14 ± 0.01	—	0.02 ± 0.01
	PI	25	Au	1635	5×10^{10}	15.29	1.68 ± 0.03	1.62 ± 0.04	2.49 ± 0.05	0.09 ± 0.00	—	0.01 ± 0.00
	PI	25	U	1975	5×10^{10}	20.01	1.76 ± 0.08	1.91 ± 0.11	2.72 ± 0.14	0.08 ± 0.01	—	0.01 ± 0.00
	PMMA	1.6	Au	185	5×10^{10}	10.87	4.92 ± 0.09	2.94 ± 0.10	6.39 ± 0.14	0.27 ± 0.01	—	0.10 ± 0.00

It is apparent that the effective track radii calculated by the different models are very similar to each other. This indicates that the Hard Cylinder Model, while it does not describe the full track structure, provides a good approximation for the track size. However, the Soft Cylinder Model can give a more detailed and realistic approximation of the track structure with computationally complex data processing. In contrast, the Core Transition Model has a better approximation of the track structure than the Hard Cylinder Model and quicker processing times than the Soft Cylinder Model. Thus, the particular requirements of the analysis will inform the selection of the most suitable model. For example, for batch fitting processes to automatically analyse a large number of *in situ* data, processing time is important. The Core Transition Model would be more suitable for this case, which is time-saving and makes the complex analysis of the structural change trend easier.[58] For the following characterization work of ion tracks, we choose the Core Transition Model for convenience.

We next investigate the ion fluence range to estimate the maximal track overlap for the applicability of the SAXS models. Higher ion fluences produce more ion tracks per area in the samples, which yield better scattering signals during SAXS

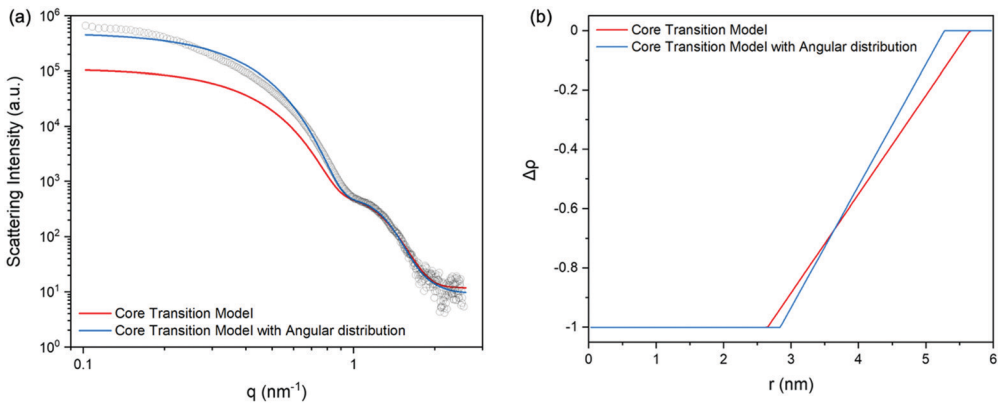

Fig. 5 (a) The effect of the angular distribution on the SAXS fitting models. For 19 μm-thick PET irradiated with 1635 MeV Au ions at 1×10^{11} ions/cm^2, SAXS patterns (circles) and corresponding fits to the Core Transition Model (red solid line) and Core Transition Model with the angular distribution (blue solid line). (b) The radial densitys variations from both fits.

 This journal is © the Owner Societies 2022

Published on 23 March 2022. Downloaded by Australian National University on 10/23/2023 8:56:24 PM.

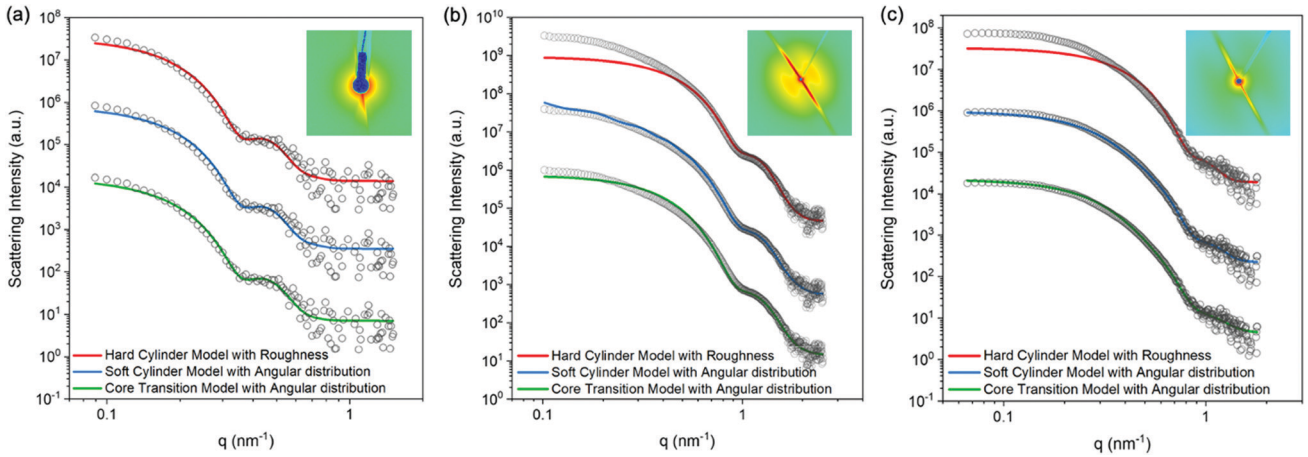

Fig. 6 SAXS patterns (circles) and corresponding fits using the Hard Cylinder Model with roughness, soft cylinder model and the Core Transition Model with the angular distribution (solid lines) for ion tracks in PET. The insets show SAXS detector images. Patterns are for (a) 2 μm-thick PET irradiated with 185 MeV Au at 1×10^{11} ions/cm^2, (b) 19 μm-thick PET irradiated with 1635 MeV Au at 1×10^{11} ions/cm^2, and (c) 2 μm-thick PET irradiated with 1635 MeV Au at 5×10^{10} ions/cm^2. Patterns are offset on the *y*-axis for clarity.

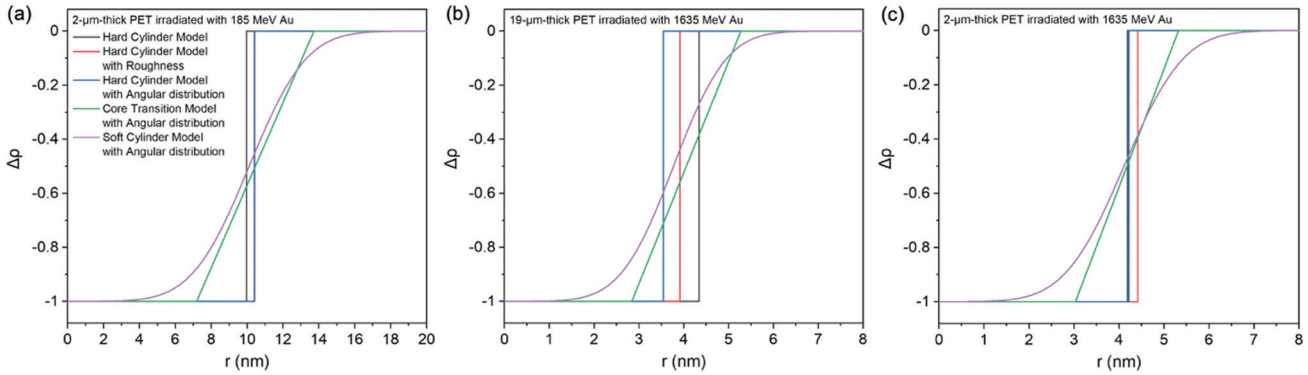

Fig. 7 Radial electron density distribution of ion tracks in PET fitted with different models. (a) 2 μm-thick PET irradiated with 185 MeV Au at 1×10^{11} ions/cm^2, (b) 19 μm-thick PET irradiated with 1635 MeV Au at 1×10^{11} ions/cm^2 and (c) 2 μm-thick PET irradiated with 1635 MeV at 5×10^{10} ions/cm^2. The density distribution of the Hard Cylinder Model with roughness and angular distribution overlap in (a).

measurements. However, there is a limit, *i.e.*, for a high degree of track overlap, the models of independent tracks described here are no longer valid. To determine the range of suitability for SAXS characterization, we used PET foils irradiated with 185 MeV Au at fluences of 5×10^{10}, 1×10^{11} and 3×10^{11} ions/cm^2 based on our previous experience, which results in track overlaps of 7.3%, 13.9%, and 34.7%, respectively.[57] The overlap is defined as the percentage of the tracks overlapping per transformed area (*i.e.*, the area covered with tracks) and the effective track radius of 9.89 nm is used for these calculations, which is obtained from the PET foil irradiated with 185 MeV Au at 5×10^{10} ions/cm^2 (Table 3). The scattering data is shown in Fig. 8a. It is evident that the scattering intensity becomes quite different when the ion fluence is increased to 3×10^{11} ions/cm^2 and the fitting curve (green solid line) does not exactly match the measured data (green circles) at higher q values ($q >$ 0.4 nm^{-1}). The track density profiles show a great similarity at fluences of 5×10^{10} and 1×10^{11} ions/cm^2, but a significant deviation at 3×10^{11} ions/cm^2 is apparent (Fig. 8b). With increasing fluence ranging from 5×10^{10} to 1×10^{11} ions/cm^2, the scattering intensity essentially scales with the fluence, but the oscillations remain the same, which indicates that the track structure remains unaffected. Thus, we consider that the amount of overlap of 14% (at a fluence of 1×10^{11} ions/cm^2) does not significantly influence the SAXS measurement and at the corresponding fluence the assumption of isolated tracks is still valid. For a fluence of 3×10^{11} ions/cm^2, where the track overlap exceeds 30%, the decreased quality of the fit indicates that the simple form factor model is not applicable anymore. These results are consistent with our previous observations on the track overlap.[75]

In addition, we compared the track structure in irradiated PET foils of different thicknesses varying from 2.8 μm to 19 μm, all of them irradiated with 1635 MeV Au at 1×10^{11} ions/cm^2. The scattering intensities are shown in Fig. 9a. Thicker samples show stronger scattering signals in the SAXS measurements due to the increased length of the tracks and thus show clearer oscillations than the thin sample (*i.e.*, 2.8 μm-thick PET). However, from the radial density profiles shown in Fig. 9b, it

Published on 23 March 2022. Downloaded by Australian National University on 10/23/2023 8:56:24 PM.

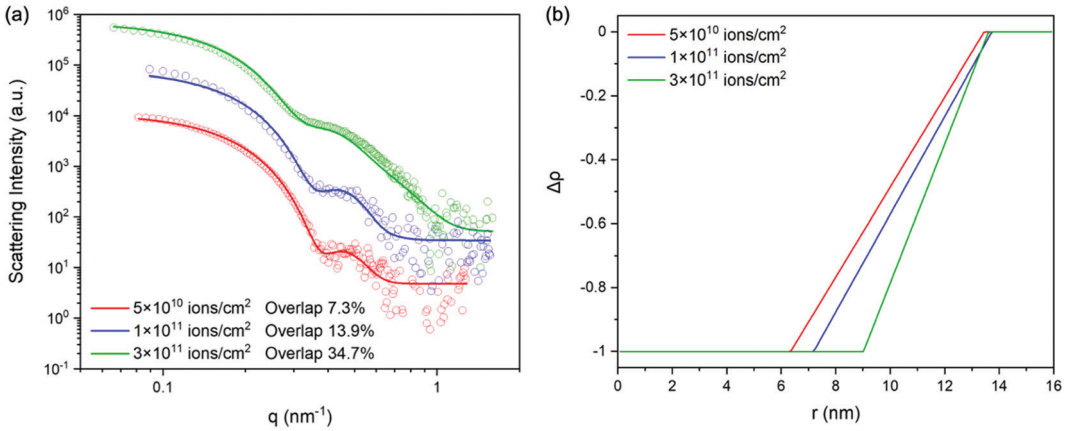

Fig. 8 (a) SAXS patterns from tracks in 2 μm-thick PET irradiated with 185 MeV Au at different fluences (circles) and corresponding fits using the Core Transition Model (solid lines). Oscillations remain similar for fluences of 5×10^{10} ions/cm^2 and 1×10^{11} ions/cm^2 and a shift towards smaller q is observed as the fluence reaches 3×10^{11} ions/cm^2. Patterns are offset on the y-axis for clarity. (b) Radial electron density profiles corresponding to (a).

is apparent that thickness does not affect the track structure within errors.

4.2 Track structure in other polymers: PC, PI and PMMA

The Core Transition Model was also applied to study ion tracks in a variety of other polymers (Table 3). The SAXS patterns of different polymers with a variety of irradiation conditions and the corresponding fits to the Core Transition Model are shown in Fig. 10. As the fits (solid lines) show, the Core Transition Model with angular distribution describes the scattering patterns for PC, PI and PMMA foils very well. The fitting parameters are listed in Table 3.

The fitting results show that the Core Transition Model works well for all polymer membranes used in our study, suggesting a gradual density change from the highly damaged track core to the undamaged polymer is inherent to the track structure of polymers. This expands the simple model of a constant low-density region in the Hard Cylinder Model to a more realistic track structure for all the investigated polymers.

Notably, the size of the core and the transition region depends on the irradiation conditions. Due to the velocity effect in swift heavy ion irradiation, as many studies previously demonstrated, low-velocity ions can produce a higher energy density than high-velocity ions, which can have a direct impact on the size of the tracks.[1,4,5,81] The values for the core and transition regions (Table 3) are consistently larger in PET and PMMA foils irradiated with 185 MeV low-velocity Au ions than that of PET and PI foils irradiated with 1635 MeV high-velocity Au ions, despite the energy loss of the latter is higher (*e.g.*, the maximum difference at the foil surface is 5.05 keV nm^{-1}). Moreover, the track size also depends on the polymer type.

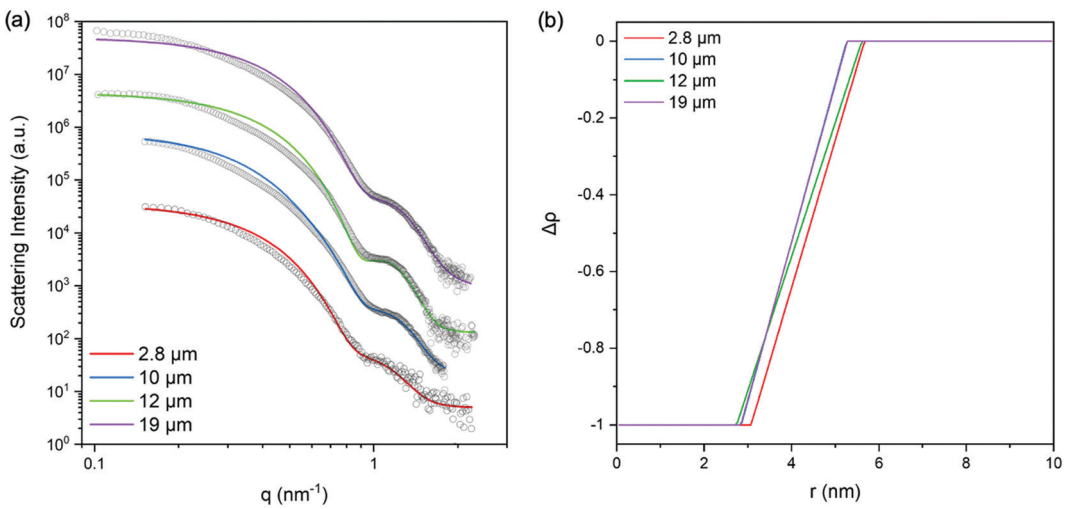

Fig. 9 SAXS measurements of PET foils with thicknesses ranging from 2.8 μm to 19 μm. (a) SAXS patterns (circles) and corresponding fits to the Core Transition Model (solid lines) for PET foils irradiated with 1635 MeV Au ions at 1×10^{11} ions/cm^2 with different thicknesses. Patterns are offset on the y-axis for clarity. (b) Radial electron density variations of ion tracks in PET under the same irradiation condition but different thicknesses (the blue line overlaps with the purple line).

 This journal is © the Owner Societies 2022

Published on 23 March 2022. Downloaded by Australian National University on 10/23/2023 8:56:24 PM.

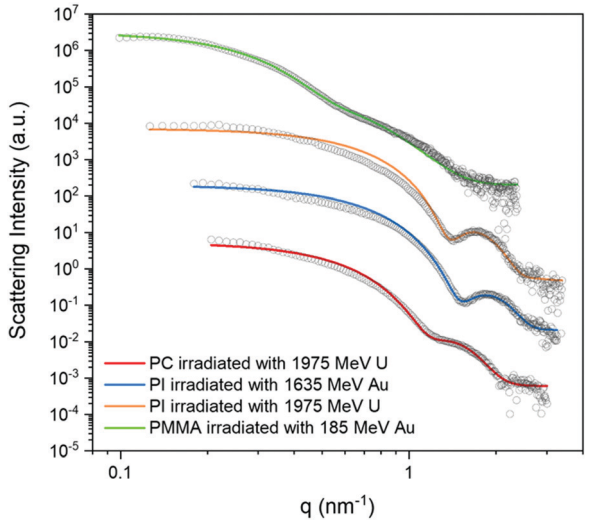

Fig. 10 SAXS patterns (circles) and corresponding fits using the Core Transition Model (solid lines) for PC, PI and PMMA irradiated with 1975 MeV U, 1635 MeV Au and 185 MeV Au at 5×10^{10} ions/cm^2, respectively. Patterns are offset on the *y*-axis for clarity.

For example, the sizes of the core and transition region of PET are bigger than those of PMMA under the same irradiation conditions (Table 3).

For inorganic insulators, the thermal-spike model suggests melting can occur inside the track core,[82–84] and the track boundary can be very sharp, for example when the track remains as an amorphous inclusion in a crystalline matrix as observed for quartz and mineral apatite.[64,65,85,86] In these cases, the transition region is insignificant, hence one would expect that the Core Transition Model is unnecessary. On the other hand, a 'Core Shell Model' has been successfully applied to show the finer structure of ion tracks in amorphous insulators like silicon dioxide, silicon nitride and silicon oxynitrides.[77,81,87,88] The radial density of the ion tracks in these materials consists of a lower density core and a higher density shell or *vice versa* as compared to the unirradiated matrix material.[74,77,87,89,90] In some cases, an extension to the model with a smooth transition between the core and shell better fits high quality SAXS data and yields an improved view of the track structure.[74] It has been suggested this is originated from the viscous flow in the molten region driven by thermal stresses arising from the non-uniform temperature profile. In contrast to inorganic materials for which the mass in the ion track is largely conserved,[91] the mass loss upon swift heavy ion irradiation is significant in polymeric materials.[1] During track formation, a series of complex chemical processes occur, such as the scission of chains, bond breakage, radical formation, crosslinking, and loss of small volatile molecules such as CO, CO_2, and H_2. This eventually leads to the formation of tracks with a lower density compared to the surrounding matrix.[1,53,92–95] This mass loss is the main difference between the track structure of polymers and inorganic insulators, and results in the required consideration of the transition region to successfully fit SAXS data for polymers.

5. Conclusions

In conclusion, SAXS is a non-destructive technique suitable for determining the structure of ion tracks in polymers which is very difficult to measure with microscopy techniques such as SEM, TEM and AFM. We developed two new fitting models, the 'Soft Cylinder Model' and the 'Core Transition Model', which fit well with the SAXS data from ion tracks in various polymer samples such as PET, PC, PI and PMMA, and describe the structure of the tracks better than the simple 'Hard Cylinder Model'. Compared with the Soft Cylinder Model, the Core Transition Model is computationally less expensive with sufficient precision due to the simplified fitting process. The more precise density distribution in the tracks revealed with the new SAXS models can provide a better understanding of the track shape and radial damage distribution inside the track. This improved method for track characterisation can further help in unravelling the mechanisms of track formation in polymers and how it depends on material properties and irradiation conditions.

Conflicts of interest

There are no conflicts to declare.

Acknowledgements

This research was undertaken at the SAXS/WAXS beamline at the Australian Synchrotron, a part of ANSTO, and we thank the beamline scientists for their technical assistance. The authors thank the UNILAC staff at GSI (Germany) for irradiation of polymer foils. The irradiated polymer foils are part of the experiment UMAT_Kluth, which was performed at the beamline X0 at the GSI Helmholtzzentrum für Schwerionenforschung (Darmstadt, Germany) in the frame of FAIR Phase-0. The authors would also like to thank the staff at the ANU Heavy Ion Accelerator Facility for their continued technical assistance. This facility is supported by the National Collaborative Research Infrastructure Strategy (NCRIS). This work was also supported by the National Natural Science Foundation of China (Grant No. 11875076) and the HIRFL funding (No. HIR19GY004). P. K. acknowledges the Australian Research Council for financial support. X. W. would like to acknowledge the China Scholarship Council for the scholarship support under the State Scholarship Fund. S. D. acknowledges support from AINSE Ltd. Postgraduate Research Award (PGRA) and Australian Government Research Training Program (RTP) Scholarship.

References

1 D. Fink, *Fundamentals of Ion-Irradiated Polymers*, Springer Science & Business Media, Berlin, Heidelberg, 2004, vol. 63.
2 C. Trautmann, Micro-and Nanoengineering with ion tracks, *Ion Beams in Nanoscience and Technology*, Springer, Berlin, Heidelberg, 2009, pp. 369–387.
3 F. F. Komarov, Nano- and microstructuring of solids by swift heavy ions, *Phys.-Uspekhi*, 2017, **60**, 435.

Published on 23 March 2022. Downloaded by Australian National University on 10/23/2023 8:56:24 PM.

4 M. Toulemonde, C. Trautmann, E. Balanzat, K. Hjort and A. Weidinger, Track formation and fabrication of nanostructures with MeV-ion beams, *Nucl. Instrum. Methods Phys. Res., Sect. B*, 2004, **216**, 1–8.
5 M. Lang, F. Djurabekova, N. Medvedev, M. Toulemonde and C. Trautmann, Fundamental Phenomena and Applications of Swift Heavy Ion Irradiations, *Comprehensive Nuclear Materials*, Elsevier, 2020, pp. 485–516.
6 P. Y. Apel, Track etching technique in membrane technology, *Radiat. Meas.*, 2001, **34**, 559–566.
7 P. Y. Apel and S. N. Dmitriev, Micro- and nanoporous materials produced using accelerated heavy ion beams, *Adv. Nat. Sci.: Nanosci. Nanotechnol.*, 2011, **2**, 013002.
8 P. Y. Apel, Fabrication of functional micro- and nanoporous materials from polymers modified by swift heavy ions, *Radiat. Phys. Chem.*, 2019, **159**, 25–34.
9 P. Y. Apel, V. V. Bashevoy, I. V. Blonskaya, N. E. Lizunov, O. L. Orelovitch and C. Trautmann, Shedding light on the mechanism of asymmetric track etching: an interplay between latent track structure, etchant diffusion and osmotic flow, *Phys. Chem. Chem. Phys.*, 2016, **18**, 25421–25433.
10 P. Y. Apel, I. V. Blonskaya, N. E. Lizunov, K. Olejniczak, O. L. Orelovitch, M. E. Toimil-Molares and C. Trautmann, Osmotic Effects in Track-Etched Nanopores, *Small*, 2018, **14**, 1703327.
11 F. Liu, M. Wang, X. Wang, P. Wang, W. Shen, S. Ding and Y. Wang, Fabrication and application of nanoporous polymer ion-track membranes, *Nanotechnology*, 2018, **30**, 052001.
12 C. Wang, Q. Fu, X. Wang, D. Kong, Q. Sheng, Y. Wang, Q. Chen and J. Xue, Atomic Layer Deposition Modified Track-Etched Conical Nanochannels for Protein Sensing, *Anal. Chem.*, 2015, **87**, 8227–8233.
13 N. Ulrich, A. Spende, L. Burr, N. Sobel, I. Schubert, C. Hess, C. Trautmann and M. E. Toimil-Molares, Conical Nanotubes Synthesized by Atomic Layer Deposition of Al_2O_3, TiO_2, and SiO_2 in Etched Ion-Track Nanochannels, *Nanomaterials*, 2021, **11**, 1874.
14 A. Spende, N. Sobel, M. Lukas, R. Zierold, J. C. Riedl, L. Gura, I. Schubert, J. M. M. Moreno, K. Nielsch, B. Stühn, C. Hess, C. Trautmann and M. E. Toimil-Molares, TiO_2, SiO_2, and Al_2O_3 coated nanopores and nanotubes produced by ALD in etched ion-track membranes for transport measurements, *Nanotechnology*, 2015, **26**, 335301.
15 M. Ali, B. Schiedt, K. Healy, R. Neumann and W. Ensinger, Modifying the surface charge of single track-etched conical nanopores in polyimide, *Nanotechnology*, 2008, **19**, 085713.
16 M. Ali, P. Ramirez, H. Q. Nguyen, S. Nasir, J. Cervera, S. Mafe and W. Ensinger, Single Cigar-Shaped Nanopores Functionalized with Amphoteric Amino Acid Chains: Experimental and Theoretical Characterization, *ACS Nano*, 2012, **6**, 3631–3640.
17 Z. Liu, W. Wang, R. Xie, X. Ju and L. Chu, Stimuli-responsive smart gating membranes, *Chem. Soc. Rev.*, 2016, **45**, 460–475.
18 G. Pérez-Mitta, M. E. Toimil-Molares, C. Trautmann, W. A. Marmisollé and O. Azzaroni, Molecular Design of Solid-State Nanopores: Fundamental Concepts and Applications, *Adv. Mater.*, 2019, **31**, 1901483.
19 G. Pérez-Mitta, J. S. Tuninetti, W. Knoll, C. Trautmann, M. E. Toimil-Molares and O. Azzaroni, Polydopamine Meets Solid-State Nanopores: A Bioinspired Integrative Surface Chemistry Approach To Tailor the Functional Properties of Nanofluidic Diodes, *J. Am. Chem. Soc.*, 2015, **137**, 6011–6017.
20 B. G. Cartwright, E. K. Shirk and P. B. Price, A nuclear-track-recording polymer of unique sensitivity and resolution, *Nucl. Instrum. Methods*, 1978, **153**, 457–460.
21 S. Kodaira, K. Morishige, H. Kawashima, H. Kitamura, M. Kurano, N. Hasebe, Y. Koguchi, W. Shinozaki and K. Ogura, A performance test of a new high-surface-quality and high-sensitivity CR-39 plastic nuclear track detector – TechnoTrak, *Nucl. Instrum. Methods Phys. Res., Sect. B*, 2016, **383**, 129–135.
22 M. E. Toimil-Molares, Characterization and properties of micro- and nanowires of controlled size, composition, and geometry fabricated by electrodeposition and ion-track technology, *Beilstein J. Nanotechnol.*, 2012, **3**, 860–883.
23 J. Duan, J. Liu, D. Mo, H. Yao, K. Maaz, Y. Chen, Y. Sun, M. Hou, X. Qu, L. Zhang and Y. Chen, Controlled crystallinity and crystallographic orientation of Cu nanowires fabricated in ion-track templates, *Nanotechnology*, 2010, **21**, 365605.
24 P. Wang, M. Wang, F. Liu, S. Ding, X. Wang, G. Du, J. Liu, P. Apel, P. Kluth, C. Trautmann and Y. Wang, Ultrafast ion sieving using nanoporous polymeric membranes, *Nat. Commun.*, 2018, **9**, 1–9.
25 Q. Wen, D. Yan, F. Liu, M. Wang, Y. Ling, P. Wang, P. Kluth, D. Schauries, C. Trautmann, P. Apel, W. Guo, G. Xiao, J. Liu, J. Xue and Y. Wang, Highly Selective Ionic Transport through Subnanometer Pores in Polymer Films, *Adv. Funct. Mater.*, 2016, **26**, 5796–5803.
26 G. Remmert, Y. Eyal, B. E. Fischer and R. Spohr, Gas permeability and cross section of latent ion tracks in polymers, *Nucl. Instrum. Methods Phys. Res., Sect. B*, 1995, **105**, 197–199.
27 V. Kulshrestha, N. Acharya, K. Awasthi, M. Singh, D. Avasthi and Y. Vijay, Study of gas permeation for asymmetric track-etched polymer blends, *Int. J. Hydrogen Energy*, 2006, **31**, 1266–1270.
28 N. K. Acharya, V. Kulshrestha, K. Awasthi, R. Kumar, A. K. Jain, M. Singh, D. K. Avasthi and Y. K. Vijay, Gas permeation study of Ti-coated, track-etched polymeric membranes, *Vacuum*, 2006, **81**, 389–393.
29 A. Kros, R. J. M. Nolte and N. A. Sommerdijk, Conducting Polymers with Confined Dimensions: Track-Etch Membranes for Amperometric Biosensor Applications, *Adv. Mater.*, 2002, **14**, 1779–1782.
30 Y. Jiang and W. Guo, Nanopore-based sensing and analysis: beyond the resistive-pulse method, *Sci. Bull.*, 2015, **60**, 491–502.
31 S. Howorka and Z. Siwy, Nanopore analytics: sensing of single molecules, *Chem. Soc. Rev.*, 2009, **38**, 2360–2384.
32 A. Mara, Z. Siwy, C. Trautmann, J. Wan and F. Kamme, An Asymmetric Polymer Nanopore for Single Molecule Detection, *Nano Lett.*, 2004, **4**, 497–501.

 This journal is © the Owner Societies 2022

Published on 23 March 2022. Downloaded by Australian National University on 10/23/2023 8:56:24 PM.

33 W. Guo, L. Cao, J. Xia, F.-Q. Nie, W. Ma, J. Xue, Y. Song, D. Zhu, Y. Wang and L. Jiang, Energy Harvesting with Single-Ion-Selective Nanopores: A Concentration-Gradient-Driven Nanofluidic Power Source, *Adv. Funct. Mater.*, 2010, **20**, 1339–1344.

34 Y. Feng, W. Zhu, W. Guo and L. Jiang, Bioinspired Energy Conversion in Nanofluidics: A Paradigm of Material Evolution, *Adv. Mater.*, 2017, **29**, 1702773.

35 H. Daiguji, P. Yang, A. J. Szeri and A. Majumdar, Electrochemomechanical Energy Conversion in Nanofluidic Channels, *Nano Lett.*, 2004, **4**, 2315–2321.

36 G. Laucirica, A. G. Albesa, M. E. Toimil-Molares, C. Trautmann, W. A. Marmisollé and O. Azzaroni, Shape matters: Enhanced osmotic energy harvesting in bullet-shaped nanochannels, *Nano Energy*, 2020, **71**, 104612.

37 W. Guo, H. Xia, F. Xia, X. Hou, L. Cao, L. Wang, J. Xue, G. Zhang, Y. Song, D. Zhu, Y. Wang and L. Jiang, Current Rectification in Temperature-Responsive Single Nanopores, *ChemPhysChem*, 2010, **11**, 859–864.

38 F. Xia, W. Guo, Y. Mao, X. Hou, J. Xue, H. Xia, L. Wang, Y. Song, H. Ji, Q. Ouyang, Y. Wang and L. Jiang, Gating of Single Synthetic Nanopores by Proton-Driven DNA Molecular Motors, *J. Am. Chem. Soc.*, 2008, **130**, 8345–8350.

39 M. Ali, P. Ramirez, S. Mafé, R. Neumann and W. Ensinger, A pH-Tunable Nanofluidic Diode with a Broad Range of Rectifying Properties, *ACS Nano*, 2009, **3**, 603–608.

40 X. Hou, W. Guo, F. Xia, F.-Q. Nie, H. Dong, Y. Tian, L. Wen, L. Wang, L. Cao, Y. Yang, J. Xue, Y. Song, Y. Wang, D. Liu and L. Jiang, A Biomimetic Potassium Responsive Nanochannel: G-Quadruplex DNA Conformational Switching in a Synthetic Nanopore, *J. Am. Chem. Soc.*, 2009, **131**, 7800–7805.

41 S. Wu, Y. Cheng, J. Ma, Q. Huang, Y. Dong, J. Duan, D. Mo, Y. Sun, J. Liu and H. Yao, Preparation and ion separation properties of sub-nanoporous PES membrane with high chemical resistance, *J. Membr. Sci.*, 2021, **635**, 119467.

42 A. Adla, H. Fuess and C. Trautmann, Characterization of heavy ion tracks in polymers by transmission electron microscopy, *J. Polym. Sci., Part B: Polym. Phys.*, 2003, **41**, 2892–2901.

43 A. Adla, V. Buschmann, H. Fuess and C. Trautmann, Investigation of heavy ion tracks in polymers by transmission electron microscopy, *Nucl. Instrum. Methods Phys. Res., Sect. B*, 2001, **185**, 210–215.

44 D. L. Zagorski, A. I. Vilensky, S. A. Kosarev, A. M. Miterev, G. S. Zhdanov and B. V. Mchedlishvili, AFM method for investigation of irradiated polymers, *Radiat. Meas.*, 2003, **36**, 233–237.

45 T. Yamauchi, N. Yasuda, T. Asuka, K. Izumi, T. Masutani, K. Oda and R. Barillon, Track core size estimation for heavy ions in CR-39 by AFM and UV methods, *Nucl. Instrum. Methods Phys. Res., Sect. B*, 2005, **236**, 318–322.

46 T. Yamauchi, D. Mineyama, H. Nakai, K. Oda and N. Yasuda, Track core size estimation in CR-39 track detector using atomic force microscope and UV-visible spectrophotometer, *Nucl. Instrum. Methods Phys. Res., Sect. B*, 2003, **208**, 149–154.

47 F. Ohnesorge and R. Neumann, Scanning force microscopy corrected for nm-scale sample elasticity on single latent heavy-ion tracks in polymers, *Europhys. Lett. EPL*, 2000, **50**, 742–748.

48 F. M. Ohnesorge, A. Müller and R. Neumann, Scanning force microscopy in a liquid on single latent ion tracks: Towards applications in polymers and atomic resolution on crystals, *Nucl. Instrum. Methods Phys. Res., Sect. B*, 2000, **166–167**, 938–943.

49 R. M. Papaléo, R. Thomaz, L. I. Gutierres, V. M. de Menezes, D. Severin, C. Trautmann, D. Tramontina, E. M. Bringa and P. L. Grande, Confinement Effects of Ion Tracks in Ultrathin Polymer Films, *Phys. Rev. Lett.*, 2015, **114**, 118302.

50 P. Y. Apel, A. Schulz, R. Spohr, C. Trautmann and V. Vutsadakis, Tracks of very heavy ions in polymers, *Nucl. Instrum. Methods Phys. Res., Sect. B*, 1997, **131**, 55–63.

51 P. Y. Apel, A. Schulz, R. Spohr, C. Trautmann and V. Vutsadakis, Track size and track structure in polymer irradiated by heavy ions, *Nucl. Instrum. Methods Phys. Res., Sect. B*, 1998, **146**, 468–474.

52 P. Y. Apel, R. Spohr, C. Trautmann and V. Vutsadakis, Track structure in polyethylene terephthalate irradiated by heavy ions: LET dependence of track diameter, *Radiat. Meas.*, 1999, **31**, 51–56.

53 T. Yamauchi, R. Barillon, E. Balanzat, T. Asuka, K. Izumi, T. Masutani and K. Oda, Yields of CO_2 formation and scissions at ether bonds along nuclear tracks in CR-39, *Radiat. Meas.*, 2005, **40**, 224–228.

54 Z. Zhu, Y. Sun, C. Liu, J. Liu and Y. Jin, Chemical modifications of polymer films induced by high energy heavy ions, *Nucl. Instrum. Methods Phys. Res., Sect. B*, 2002, **193**, 271–277.

55 H. Schnablegger and Y. Singh, *The SAXS guide: getting acquainted with the principles*, Austria, Anton Paar GmbH, 2011.

56 I. W. Hamley, *Small-angle scattering: theory, instrumentation, data and applications*, John Wiley & Sons, 2021.

57 U. H. Hossain, M. D. Rodriguez, D. Schauries, A. Hadley, M. Schleberger, C. Trautmann, S. Mudie and P. Kluth, SAXS investigation of un-etched and etched ion tracks in polycarbonate, *Nucl. Instrum. Methods Phys. Res., Sect. B*, 2017, **409**, 293–297.

58 A. Kiy, C. Notthoff, S. Dutt, M. Grigg, A. Hadley, P. Mota-Santiago, N. Kirby, C. Trautmann, M. E. Toimil-Molares and P. Kluth, Ion track etching of polycarbonate membranes monitored by in situ small angle X-ray scattering, *Phys. Chem. Chem. Phys.*, 2021, **23**, 14231–14241.

59 T. W. Cornelius, B. Schiedt, D. Severin, G. Pépy, M. Toulemonde, P. Y. Apel, P. Boesecke and C. Trautmann, Nanopores in track-etched polymer membranes characterized by small-angle x-ray scattering, *Nanotechnology*, 2010, **21**, 155702.

60 G. Pépy, P. Boesecke, A. Kuklin, E. Manceau, B. Schiedt, Z. Siwy, M. Toulemonde and C. Trautmann, Cylindrical nanochannels in ion-track polycarbonate membranes studied by small-angle X-ray scattering, *J. Appl. Crystallogr.*, 2007, **40**, s388–s392.

Published on 23 March 2022. Downloaded by Australian National University on 10/23/2023 8:56:24 PM.

61 M. Engel, B. Stühn, J. J. Schneider, T. Cornelius and M. Naumann, Small-angle X-ray scattering (SAXS) off parallel, cylindrical, well-defined nanopores: from random pore distribution to highly ordered samples, *Appl. Phys. Mater. Sci. Process.*, 2009, **97**, 99–108.
62 D. Schauries, P. Mota-Santiago, E. P. Gilbert, N. Kirby, C. Trautmann and P. Kluth, Structure, morphology and annealing behavior of ion tracks in polycarbonate, *Eur. Polym. J.*, 2018, **108**, 406–411.
63 D. Schauries, M. D. Rodriguez, B. Afra, T. Bierschenk, C. Trautmann, S. Mudie and P. Kluth, Size characterization of ion tracks in PET and PTFE using SAXS, *Nucl. Instrum. Methods Phys. Res., Sect. B*, 2015, **365**, 573–577.
64 B. Afra, M. D. Rodriguez, M. Lang, R. C. Ewing, N. Kirby, C. Trautmann and P. Kluth, SAXS study of ion tracks in San Carlos olivine and Durango apatite, *Nucl. Instrum. Methods Phys. Res., Sect. B*, 2012, **286**, 243–246.
65 B. Afra, M. D. Rodriguez, C. Trautmann, O. H. Pakarinen, F. Djurabekova, K. Nordlund, T. Bierschenk, R. Giulian, M. C. Ridgway, G. Rizza, N. Kirby, M. Toulemonde and P. Kluth, SAXS investigations of the morphology of swift heavy ion tracks in α-quartz, *J. Phys.: Condens. Matter*, 2013, **25**, 045006.
66 N. A. Medvedev, R. A. Rymzhanov and A. E. Volkov, Time-resolved electron kinetics in swift heavy ion irradiated solids, *Appl. Phys.*, 2015, **48**, 355303.
67 T. Kusumoto, R. Barillon, S. Okada, T. Yamauchi and K. Satoshi, Improved criterion of the mechanism for forming latent tracks in poly(allyl diglycol carbonate) based on the number of interactions induced by secondary electrons, *Radiat. Meas.*, 2020, **138**, 106445.
68 D. Albrecht, P. Armbruster, R. Spohr, M. Roth, K. Schaupert and H. Stuhrmann, Investigation of heavy ion produced defect structures in insulators by small angle scattering, *Appl. Phys. Solids Surf.*, 1985, **37**, 37–46.
69 S. A. Saleh and Y. Eyal, Porous tracks along wakes of swift uranium ions in polyimide, *Appl. Phys. Lett.*, 2004, **85**, 2529–2531.
70 S. A. Saleh and Y. Eyal, Structure of Latent Heavy Ion Tracks in Polyimide, *Mol. Cryst. Liq. Cryst.*, 2006, **448**, 233–242.
71 M. Fromm, S. Kodaira, T. Kusumoto, R. Barillon and T. Yamauchi, Role of intermediate species in the formation of ion tracks in PADC: A review, *Polym. Degrad. Stab.*, 2019, **161**, 213–224.
72 V. Hnatowicz, J. Vacik and P. Y. Apel, On the structure of etched ion tracks in polymers, *Radiat. Phys. Chem.*, 2016, **121**, 106–109.
73 J. F. Ziegler, M. D. Ziegler and J. P. Biersack, SRIM – The stopping and range of ions in matter (2010), *Nucl. Instrum. Methods Phys. Res., Sect. B*, 2010, **268**, 1818–1823.
74 P. Mota-Santiago, H. Vazquez, T. Bierschenk, F. Kremer, A. Nadzri, D. Schauries, F. Djurabekova, K. Nordlund, C. Trautmann, S. Mudie, M. C. Ridgway and P. Kluth, Nanoscale density variations induced by high energy heavy ions in amorphous silicon nitride and silicon dioxide, *Nanotechnology*, 2018, **29**, 144004.
75 S. Dutt, P. Apel, N. Lizunov, C. Notthoff, Q. Wen, C. Trautmann, P. Mota-Santiago, N. Kirby and P. Kluth, Shape of nanopores in track-etched polycarbonate membranes, *J. Membr. Sci.*, 2021, **638**, 119681.
76 D. S. Sivia, *Elementary scattering theory: for X-ray and neutron users*, Oxford University Press, Oxford, New York, 2011.
77 P. Kluth, C. S. Schnohr, O. H. Pakarinen, F. Djurabekova, D. J. Sprouster, R. Giulian, M. C. Ridgway, A. P. Byrne, C. Trautmann, D. J. Cookson, K. Nordlund and M. Toulemonde, Fine Structure in Swift Heavy Ion Tracks in Amorphous SiO_2, *Phys. Rev. Lett.*, 2008, **101**, 175503.
78 P. Kluth, C. S. Schnohr, D. J. Sprouster, A. P. Byrne, D. J. Cookson and M. C. Ridgway, Measurement of latent tracks in amorphous SiO_2 using small angle X-ray scattering, *Nucl. Instrum. Methods Phys. Res., Sect. B*, 2008, **266**, 2994–2997.
79 G. Pépy, New two-dimensional data treatment software for small-angle scattering, *J. Appl. Crystallogr.*, 2007, **40**, s433–s438.
80 M. Engel and B. Stühn, *In situ* small angle X-ray scattering measurements of the filling process of polyisobutylene and poly-ε-caprolactone in ion track etched polycarbonate nanopores, *J. Chem. Phys.*, 2010, **132**, 224502.
81 C. Dufour and M. Toulemonde, in *Ion Beam Modification of Solids*, ed. W. Wesch and E. Wendler, Springer International Publishing, Cham, 2016, pp. 63–104.
82 E. M. Bringa and R. E. Johnson, Coulomb Explosion and Thermal Spikes, *Phys. Rev. Lett.*, 2002, **88**, 165501.
83 M. Toulemonde, C. Dufour and E. Paumier, Transient thermal process after a high-energy heavy-ion irradiation of amorphous metals and semiconductors, *Phys. Rev. B: Condens. Matter Mater. Phys.*, 1992, **46**, 14362–14369.
84 M. Toulemonde, C. Dufour, A. Meftah and E. Paumier, Transient thermal processes in heavy ion irradiation of crystalline inorganic insulators, *Nucl. Instrum. Methods Phys. Res., Sect. B*, 2000, **166–167**, 903–912.
85 A. Nadzri, D. Schauries, P. Mota-Santiago, S. Muradoglu, C. Trautmann, A. J. W. Gleadow, A. Hawley and P. Kluth, Composition dependent thermal annealing behaviour of ion tracks in apatite, *Nucl. Instrum. Methods Phys. Res., Sect. B*, 2016, **379**, 211–214.
86 D. Schauries, *Ion Tracks in Apatite and Quartz: And Their Behaviour with Temperature and Pressure*, Springer International Publishing, Cham, 2018.
87 P. Mota-Santiago, D. Schauries, A. Nadzri, K. Vora, M. C. Ridgway and P. Kluth, Characterization of ion track morphology formed by swift heavy ion irradiation in silicon oxynitride films, *EPJ Web Conf.*, 2015, **91**, 00008.
88 M. Lang, Advances in understanding of swift heavy-ion tracks in complex ceramics, *Curr. Opin. Solid State Mater. Sci.*, 2015, **19**, 39–48.
89 M. C. Ridgway, T. Bierschenk, R. Giulian, B. Afra, M. D. Rodriguez, L. L. Araujo, A. P. Byrne, N. Kirby, O. H. Pakarinen, F. Djurabekova, K. Nordlund, M. Schleberger, O. Osmani, N. Medvedev, B. Rethfeld and P. Kluth, Tracks and Voids in Amorphous Ge Induced by

 This journal is © the Owner Societies 2022

Published on 23 March 2022. Downloaded by Australian National University on 10/23/2023 8:56:24 PM.

Swift Heavy-Ion Irradiation, *Phys. Rev. Lett.*, 2013, **110**, 245502.

90 P. Kluth, O. H. Pakarinen, F. Djurabekova, R. Giulian, M. C. Ridgway, A. P. Byrne and K. Nordlund, Nanoscale density fluctuations in swift heavy ion irradiated amorphous SiO_2, *J. Appl. Phys.*, 2011, **110**, 123520.

91 O. H. Pakarinen, F. Djurabekova and K. Nordlund, Density evolution in formation of swift heavy ion tracks in insulators, *Nucl. Instrum. Methods Phys. Res., Sect. B*, 2010, **268**, 3163–3166.

92 V. Kumar, B. Chaudhary, V. Sharma and K. Verma, *Radiation Effects in Polymeric Materials*, ed. Springer International Publishing, Cham, 2019.

93 R. Thomaz, P. Louette, G. Hoff, S. Müller, J. J. Pireaux, C. Trautmann and R. M. Papaléo, Bond-Breaking Efficiency of High-Energy Ions in Ultrathin Polymer Films, *Phys. Rev. Lett.*, 2018, **121**, 066101.

94 T. Kusumoto, Y. Mori, M. Kanasaki, T. Ueno, Y. Kameda, K. Oda, S. Kodaira, H. Kitamura, R. Barillon and T. Yamauchi, Yields on the formation of OH groups and the loss of CH groups along nuclear tracks in PADC films, *Radiat. Meas.*, 2015, **83**, 59–62.

95 Y. Mori, T. Yamauchi, M. Kanasaki, Y. Maeda, K. Oda, S. Kodaira, T. Konishi, N. Yasuda and R. Barillon, Radiation chemical yields for loss of ether and carbonate ester bonds in PADC films exposed to proton and heavy ion beams, *Radiat. Meas.*, 2011, **46**, 1147–1153.